Three-dimensional radiometric aperture synthesis microscopy for security screening

Neil A. Salmon*, Nick Bowring
Manchester Metropolitan University, Manchester, M15 6BH, UK

ABSTRACT

The three dimensional (3D) aperture synthesis imaging technique investigated here is a generalisation of the classic two-dimensional radio astronomy technique with refinements for the near-field so it can be applied a personnel security screening portal. This technique can be viewed as a novel form of diffraction emission tomography and extends previous 3D aperture synthesis imaging research using matrix inversion techniques [1]. Simulations using three-dimensional Fourier transforms to create three-dimensional images from simulated three-dimensional visibility functions illustrate the Abbe microscopy resolution should be achievable in three dimensions simultaneously in a single sensor. The field-of-view is demonstrated to be limited by Fresnel scale effects and a means to over coming this by processing sub-sets of local visibility functions with different phase centres throughout the imaging volume is presented. The applications of this technique to a full 3D imaging security screening portal is explored and a route to extending simulation software for market driven imaging scenarios is discussed.

Keywords: Aperture synthesis, imaging, tomography, three-dimensional, millimetre wave, security, near-field, microscopy

1. INTRODUCTION

The van Cittert Zernike theorem[8][9][10] is the basic theory which underpins the radio astronomy aperture synthesis technique, which has been used for many decades to create two-dimensional (2D) images of astrophysical subjects on the celestial sphere [11]. Over the past 30 years passive millimetre wave imaging has been the subject of technology development for security screening applications and all-weather imaging [2]. The commercialisation of millimetre wave imaging has been stunted by the large physical volumes of demonstrator systems, limited depths of fields arising from optical aberrations and false alarms due to artefacts associated with illumination. The aperture synthesis approach to PMMW imaging offers a route to a compact and conformally deployable sensor (for integration into the confined spaces of entrances and bonded to the skins of aircraft), which is free from optical aberrations, is not limited by depth of field and uses spatially incoherent illumination to minimise false alarms [1][5][6][7]. By extending the 2D aperture synthesis technique to 3D it is shown how a full 3D imaging capability can be achieved which is ideally suited to security screening portal applications.

2. THREE DIMENSIONAL IMAGE CREATION

2.1 Image creation in 3D

The 3D images are created from the 3D a visibility function by taking the Fourier transform of the 3D visibility function. Mathematically this is given by Eq. 1, which is the 3D analogue of the 2D technique [11], where $A(l,m,n)$ is the average antenna pattern, (l,m,n) are the direction cosines, $V(u,v,w)$ is the near-field 3D visibility function [12], constructed from the cross-correlations from the pairs of receivers phase corrected to form a 3D image around a particular phase centre in space. The u,v,w are the local spatial frequency components [12] [17] of the image measured across the baselines of the antenna array in the respective x,y,z directions.

* Correspondence: Email: n.salmon at mmu.ac.uk; Telephone: +44 7921172892

$$I(l,m,n)=\frac{1}{A(l,m,n)}\int_{w_{MIN}}^{w_{MAX}}\int_{v_{MIN}}^{v_{MAX}}\int_{u_{MIN}}^{u_{MAX}}V(u,v,w)e^{+j2\pi(ul+vm+wn)}du\,dv\,dw \tag{1}$$

To examine if this technique works, the images of point sources were created by taking the 3D Fourier transforms of the visibility functions modified for the near-field. These were then used to determine the spatial resolution and field of view of the technique in 3D space. As this technique uses the fast Fourier transform to calculate the 3D Fourier transforms it is much faster and requires far less memory that the previous 3D aperture synthesis inversion algorithms using matrix inversions, described in Ref. [1].

2.2 3D point spread functions

An important property of an imaging system is the point spread function PSF. This quantity determines the sharpness of images generated by the system and hence the maximum number of pixels and information content within the image. The image generated by a system is the convolution of objects in the scene with the point spread function. The PSF of a system can be simulated (or measured) by generating the image of a synthetic delta function (or a point noise source).

The 3D PSF of the hypothetical 3D spherical antenna array having a diameter of 1 m and with 300 antennas operating at 22.51 GHz was calculated using the following algorithm: 1) synthetic cross-correlations were created [1] from a delta function source at the centre of the array volume; 2) these were used to create a near-field Hermitian 3D visibility function; 3) a 3D Fourier transform of this was taken to create the 3D image. The PSF which results from this is a 3D real quantity. As visualisation of 3D functions is non-trivial, perhaps the best way of viewing these is to display three surface plots in different planes. The planes chosen in this particular instance are those through the centre of the imaging volume in directions: *y-x*, *z-x* and the *y-z*, as presented in Figure 1. These images illustrate that the 3D PSF is symmetrical in 3D space about the centre of the spherical antenna array.

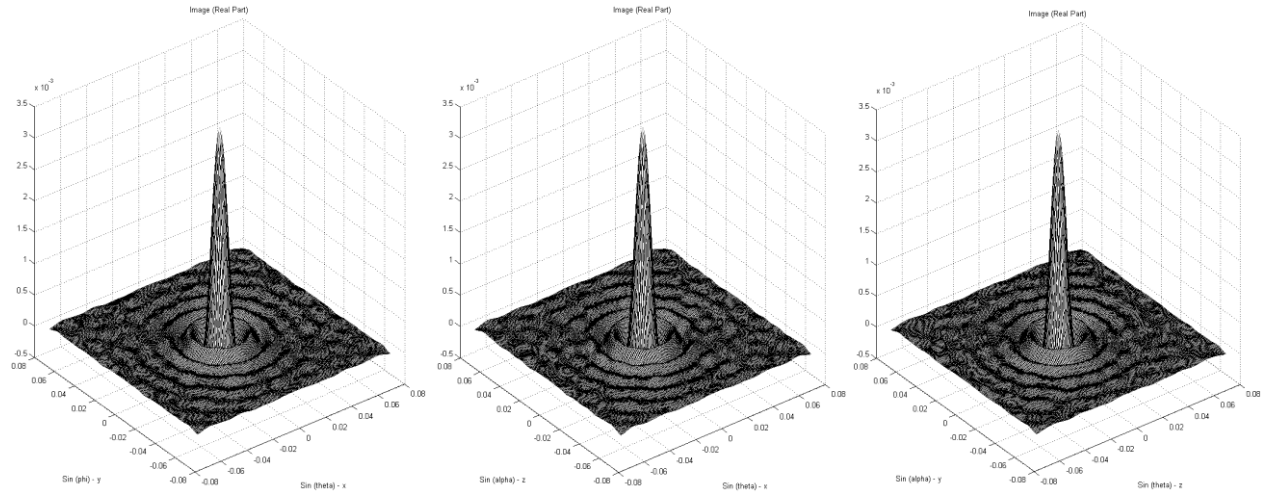

Figure 1. Cross-sections of the 3D point spread function through the central y-x, z-x, y-z planes (left to right) from an aperture synthesis spherical imaging array1. The functions are approximately Bessel function, J_1(r/r) shaped.

2.3 Rayleigh resolution

Closer scrutiny of the PSF can be had by an examination of the side view of the PSF and an image of the natural logarithm of the absolute value of the function, and these are shown in Figure 2 for the PSF through the central *x-y* plane. The images through the other *x-z* and *z-y* planes are nominally identical. The side view indicates there are some small negative values around the first minimum, but the total area under the curve appears to be positive. Negative values in a PSF are something which cannot exist for a focal plane based quasi-optical imager, but are allowed in an aperture synthesis imaging system. This is because the aperture synthesis does not sample directly in the image plane, but in the spatial frequency domain. The PSF surface plots appear qualitatively to have a $J_1(r)/r$ form where $J_1(r)$ is the Bessel function of the first kind, order 1, and *r* is the coordinate moving out from the centre of the function. However they differ

from the Airy function associated with the diffraction from the circular aperture of a classical imaging system due to the negative values.

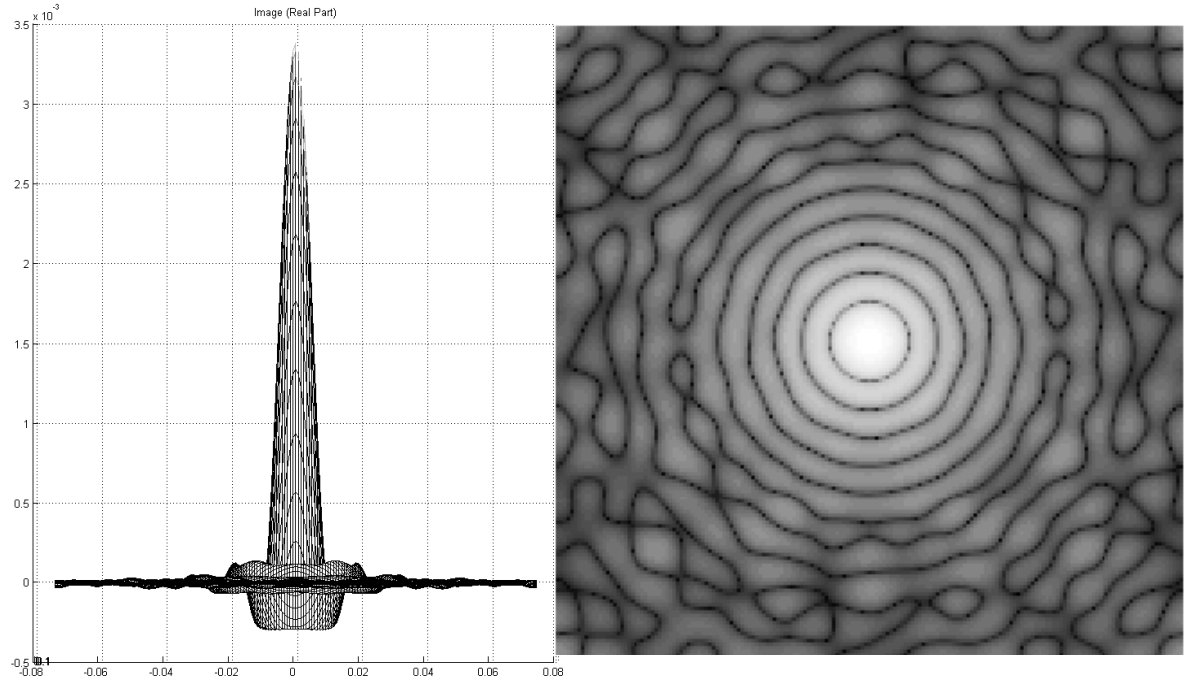

Figure 2. The Rayleigh resolution limit (first minima in the PSF) illustrated here with an end view of the surface plot of the *x-y* slice through the 3D point spread function (left) and an image of the logarithm of the absolute value of this function, from the receiver array of Figure 1, is very close the Abbe limit.

The log image of the PSF indicates the zero crossings as dark circles around the main lobe. From an examination of the width of this function, the first zero crossing is at λ/2.66 and the first minima, which is by definition the Rayleigh resolution [14], is at λ/2.09, with a measurement error 10%. The first minima can be seen as the peak intensity of the first bright ring in the PSF log image plot in Figure 2. The Rayleigh resolution found here is very close to the Abbe resolution limit for microscopy. The Abbe limit indicates the highest possible resolution achievable when using a lens and incoherent illumination, and is given by Eq. 2, where *n* is the refractive index of the media in which the subject is located and θ is the angle subtended at subject by the objective lens of the imaging system. This does perhaps suggest that an aperture synthesis approach to microscopy might offer something like a 9% improvement in resolution. The higher refractive index of materials therefore improved the resolving power of the instrument, property that is regularly exploited in microscopy.

$$d_{min\_NF} = \frac{\lambda}{2n\sin\theta} \qquad (2)$$

$$d_{min\_FF} = 1.22\frac{\lambda}{D}R \qquad (3)$$

2.4 Rayleigh resolution in the far-field for comparison

For resolution comparisons with the far field, the PSF was investigated in a similar fashion. Using the spherical antenna array, but turning all antennas to look outwards to a point source placed at a range, *R* of 1.5 km the first minimum of the image was found at a distance of $\sim(R/1.09).(\lambda/D)$ from the central peak, where *D* is the array diameter (1 m in this case). Changing the array to a 2D circular array made little difference to this resolution. This resolution can be compared to the first minimum of the Airy function which from classical optics [10] is given by Eq. 3. This corresponds to the Rayleigh resolution in the far field for a fully filled circular aperture lens based imager. This demonstrates that the far field the aperture synthesis imager has a Rayleigh resolution 10% smaller than that of the quasi-optical counterpart. These resolution limits are summarised in Table 1.

2.5 Sparrow Resolution

Another resolution criterion that has been evaluated for the 3D imaging is the Sparrow resolution limit [14]. This is useful if the PSFs don't have a well-defined first minimum [14]. The Sparrow resolution is usually just slightly smaller than the Rayleigh resolution for many optical systems. According to Sparrow two peaks are just resolved when there just becomes a minimum between them. This can be simulated by forming the image of two delta functions and then bringing them together until there is a very small minimum between the two. This is referred to in this document as the Double-Delta Function (DDF) test for Sparrow resolution. For a separation in the x-direction the simulation of this scenario is shown as a surface plot and an image in Figure 3. Analysis indicated that Sparrow resolution limit is $\lambda/2.21 \pm 10\%$ and is symmetrical in *x, y* and *z* directions, although for brevity only the *x-y* plane is shown in the figure.

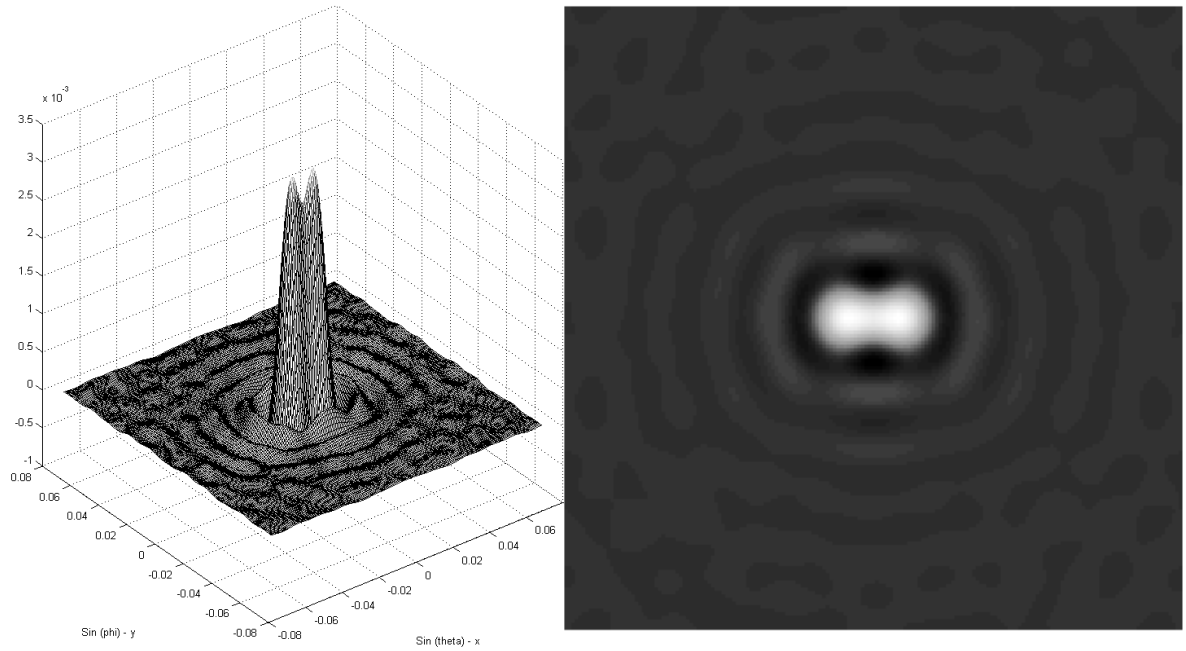

Figure 3. The Sparrow resolution limit for the 1m diameter spherical imaging array 1 indicates the 3D imaging resolution is $\lambda/2.21 \pm 10\%$.

2.6 Potential in-body screening for medical and security applications at lower frequencies (<4 GHz)

As higher media refractive indices, effectively compress the wavelength, this might be useful when imaging inside the human body for security or medical applications. For radiation to penetrate the body the frequency must be in the GHz region, where for example at a frequency of 3 GHz the free-space wavelength is 10 cm and the human body refractive index varies from 5 to 10 and is dependent on tissue [15]. Given the above determined Sparrow resolution for this architecture of imager, a spatial resolution in 3D space of between 5 mm and 10 mm may be possible in the human body. Given the radiation penetration depths in human tissue from Ref. [15] is up to a maximum of about 5 cm, a few depth pixels of 3D imagery may be possible just below the surface of the skin. The medical opportunity for 3D thermography, using aperture synthesis, was insightfully highlighted in Ref.[19], at a time before digital cross-correlators had anything like the performance they have now to realise these capabilities in a demonstrator.

2.7 Sparrow resolution in the far-field for comparison

For resolution comparisons in the far field the double delta function (DDF) approach to determining the Sparrow resolution limit was investigated in a similar fashion. Using the array of Figure 1 a DDF was placed at a range of, *R* of 1.5 km and imaged. The Sparrow spatial resolution from this simulation was found to be ~.$(R/1.14).(\lambda/D)$. By comparison the Sparrow resolution for a fully filled lens based imager in the far field is $(R/1.052).(\lambda/D)$ from Ref. [14]. This suggests the aperture synthesis Sparrow resolution limit is 8% better than that from a lens based imager. These resolutions are summarised in Table 1.

2.8 Spatial Resolutions at other frequencies and larger sized arrays

So far the spatial resolution was investigated at a frequency of 22.51 GHz and for the spherical array, which has a diameter of 1 m. However, with validated software the resolution was investigated at additional frequencies and for spherical arrays of different diameters. In summary for an array of diameter 60 cm, using the above DDF technique, the Sparrow resolution was found to be 3.35 cm (3.71 GHz), 6 mm (22.51 GHz) and 0.4 mm (320 GHz). These other frequencies were chosen as the two lower frequencies are close to the frequencies of existing experimental systems and the higher frequency (320 GHz) is perhaps the highest that would be used for security screening of personnel, the capability being limited at the higher frequencies by scattering due to clothing weave. The array diameter was also varied between 30 cm and 2 m and in all cases the Sparrow resolution was determined to be ~ λ/2.2.

	Near field	Far field
Rayleigh resolution (from PSF)	$\sim\frac{\lambda}{2.0897}$	$\sim\frac{R}{1.09}\left(\frac{\lambda}{D}\right)$
Sparrow resolution (from DDF)	$\sim\frac{\lambda}{2.21}$	$\sim\frac{R}{1.14}\left(\frac{\lambda}{D}\right)$

Table 1. Rayleigh and Sparrow resolutions for the 1 m aperture diameter imaging array, determined by simulation. In all cases the resolutions are slightly superior to classic accepted values for quasi-optical (lens or mirror based focal plane array imaging) systems.

2.9 Imaging away from the from the phase centre of the array

A question to be answered is how well does the 3D imaging technique work when the subject is not in the central region of the imager. This question can partly be answered by performing a simulation of a point source that has been displaced away from the central position. This has been done for a 3 cm displacement of point source from the array centre, whilst keeping the phase centre of the visibility functions at the centre of the array. The results of moving the point source separately in the x, y, z directions are illustrated in Figure 4, by showing a *x-y*, *x-y* and *y-z* slices through the 3D image. These images indicate that the inversion code is correctly reproducing the displacement of the point source away from the centre of the array imaging volume and that the shape of the function continues to be Bessel function like.

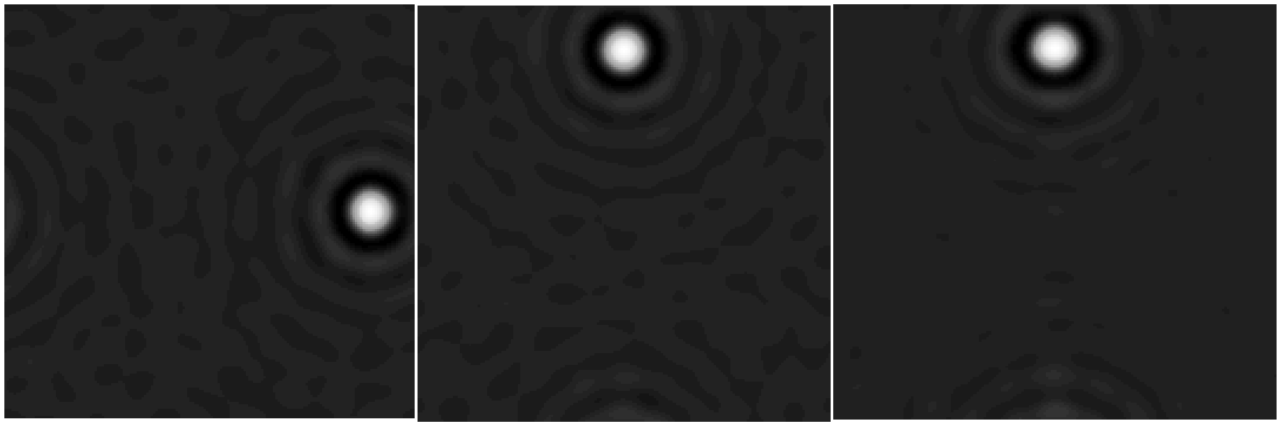

Figure 4. Slices in in the *x-y*, *x-y* and *y-z* planes (from left to right) through the simulated 3D images of a delta function that has been moved a distance of 3 cm from the phase centre at the centre of the array in respective *x*, *y* and z directions. These images confirm the viability of the 3D aperture synthesis technique.

2.10 The 3D field of view

The algorithm used in this imaging technique involves taking the 3D Fourier transform of a near-field modified 3D visibility function. From the theory of near-field imaging in the Fresnel regime, the field of view is restricted to a width of $4\sqrt{(\lambda R)}$, where R is the range of the subject [18]. In the case of array of receivers in Figure 1 this range is the radius of the spherical array. The distance $\sqrt{(\lambda R)}$ is sometimes referred to as the Fresnel scale, as emphasised in Eq. 4. In view of this limitation it is useful to investigate the field of view using this imaging algorithm.

$$Fresnel\ scale = \sqrt{\lambda R} \tag{4}$$

The field of view may be investigated by imaging three delta functions. These are basically two delta functions equally spaced around a third central delta function which is placed at the centre of the array. These three delta functions are then run through the imaging algorithm. The distance between the delta functions is then increased and as this is done the amplitude of the two outer delta functions becomes reduced in the resulting processed image. When the amplitude of the outer delta functions has fallen to 50% of the central delta function, the field of view limit has been reached. This technique is referred to in this document as the Triple Delta Function (TDF) determination of the full field of view. An example of this scenario is illustrated in Figure 5. Analysis of the fields-of-view in the y-z and z-x planes shows identical results.

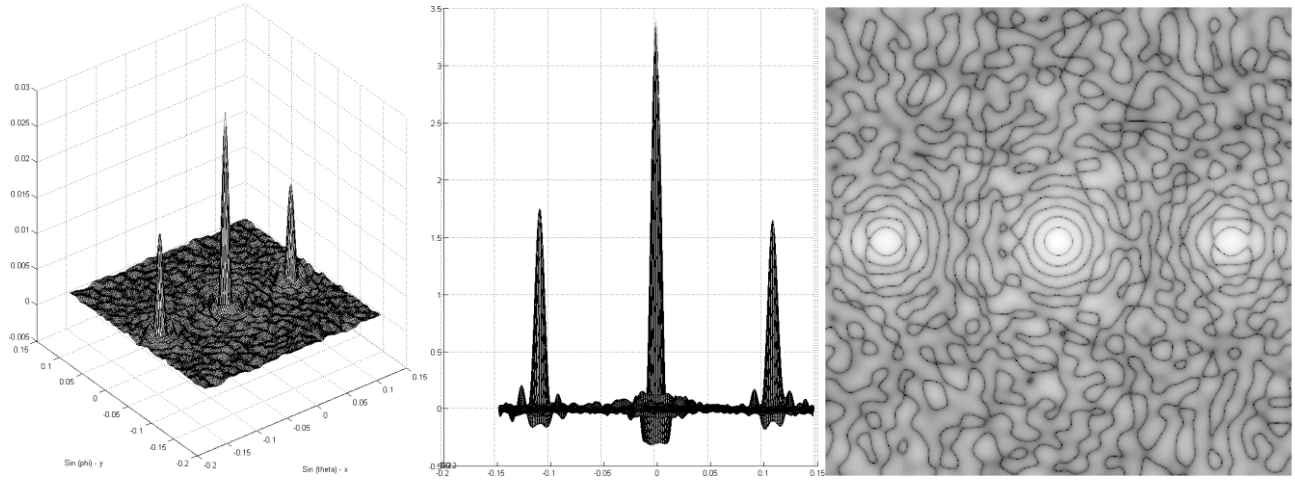

Figure 5. The Triple Delta Function test determined the field of view when the outer two delta functions have 50% of the amplitude of the centre one. The scenario is depicted above showing from left to right: A surface plot to illustrate the general shape of the image; an end view of the surface plot to illustrate the negative values and the relative magnitudes of the peaks; an image of the logarithm of the absolute values to shown general structure.

From these simulations it is clear that the field of view is limited by this algorithm. Further simulations were carried out using a spherical array, but one which had a diameter was 60 cm, just to reduce computation time, which for each image was a couple of minutes running the interpreter based language. For this particular array the field of view was determined for the frequencies of 3.71 GHz, 22.51 GHz and 320 GHz. The fields of views determined by this method are summarised in Table 2.

Frequency	3.71 GHz	22.51 GHz	320 GHz
Wavelength λ	8.08 cm	1.33 cm	0.937 mm
Field of view	28 cm	11 cm	1.67 cm
Fresnel Scale √(λR)	15 cm	6.32 cm	1.67 cm

Table 2. The full field of views, as determined by the Triple Delta Function technique, and the Fresnel scales for a spherical array of receiver 60 cm in diameter for the frequencies of 3.71 GHz, 22.51 GHz and 320 GHz.

Analysis of the results in Table 2 indicate that the field of view is reduced at the higher frequencies, as would be expected from the decrease of the Fresnel scale, arising from the Fresnel approximation used in the algorithm. The field of view is found to be symmetrical. This investigation indicates the full field of view is between one and 1.8 Fresnel scales.

Given the volume imaged is limited by the Fresnel Scale and that spatial resolution is defined by the Abbe resolution the number of voxels within this imaging volume is given approximately by Eq. 5. This for example with the 1 m diameter array (R=50 cm) at 22.51 GHz the number of voxels is approximately 1844.

$$No\ of\ voxels \approx \left(\frac{Fresnel\ Scale}{Abbe\ Resolution} \right)^3 = 8\left(\frac{R}{\lambda} \right)^{3/2} \tag{5}$$

2.11 Imaging the full volume in a security screening portal

For a given 3D Fourier transform the number of voxels in the resulting 3D image is limited approximately to that given by Eq. 5, this limitation being demonstrated in the previous paragraph. However, the volume that is imaged can be moved to any location, by the movement of the phase centre to the centre of the region of interest. A full region of 3D

space within a security screening portal can therefore be constructed from a set of 3D Fourier transforms on visibilities tuned to the different regions of space. The full image can then be mosaicked from the set of separate 3D images.

In practice however, at least for security screening, the effective number of voxels which are filled with emission is reduced to that thin layer around the surface a person. This is because in the millimetre band voxels inside that body cannot radiate to the outside world, as human tissue is too attenuating, and the volumes around a person cannot radiation, as emissivity of air is insufficiently high. For a portal, the algorithm needs to generate the 3D images around the surface of the person, the area of an average person being 1.8 m^2.

Further economising measures may be made, as cross correlations will be zero for those pairs of antennas where there is no common target area, in the case of opaque targets. This means a full set of cross-correlations from all antenna-receiver pairs will not be processed, only sub-sets or clusters will be processed.

The ability to image in 3D around the surface of the human body means that depth information will be available where clothing might be particularly thick, in such places where threats may be concealed. This depth profile offers an extra discriminant for security screening of personnel.

2.12 Simulation of a full 3D security screening portal

In view of limitations set by the Fresnel scale, a simulation at 22 GHz of a 2D Vitruvian Man subject image only 30 cm tall, but positioned at the centre of the 2 m diameter spherical array. Being 2D the subject can be considered similar to a cardboard cut-out, in that there is no depth to the subject. The original subject image is resampled at the near-field Sparrow resolution limit of (λ/2.21 ~ 6 mm) from Table 1 (to minimise computation time in generating the synthetic cross-correlations) and this is shown in Figure 6. From the synthetic cross-correlations the 3D visibility function was constructed consisting of 113x113x113 complex elements which was 3D Fourier transformed to generate the 3D images of the interior of the security screening portal.

Three central slices of this 3D image are shown in Figure 6, one in the z-y plane (the side view), one in the x-y plane (the front view) and one in the y-z plane (the top view). The hands and feet in the front view image are faded in contrast and spurious background artefacts are present due to Fresnel scale effects. However, the general overall shape of the subject is reproduced. The top view slice image correctly identifies the subject to be one in only 2D, as only a single white lines are seen in the side and top view images; the cardboard cut-out effectively has no depth.

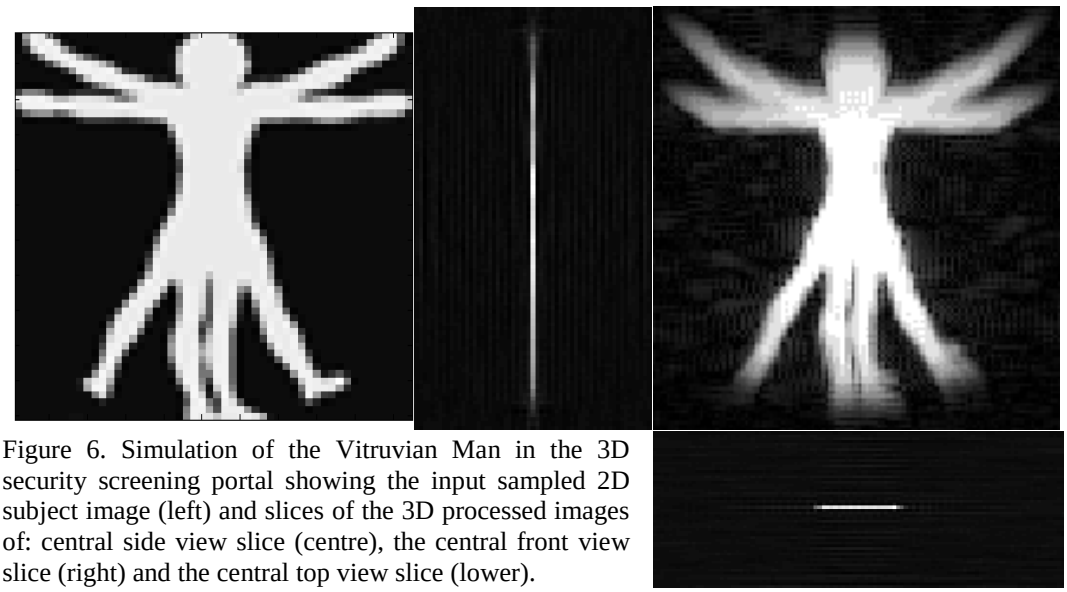

Figure 6. Simulation of the Vitruvian Man in the 3D security screening portal showing the input sampled 2D subject image (left) and slices of the 3D processed images of: central side view slice (centre), the central front view slice (right) and the central top view slice (lower).

Future developments of the software will implement hidden facet removal in the generation of synthetic cross-correlations from 3D subjects. A single set of cross-correlations will be broken down into subsets, creating separate 3D visibility functions, one for each local region of space in the portal and each with a phase centre at the centre of that space. Separate 3D images with be created by running the 3D Fourier transform on each local visibility function. The resulting images will then be mosaicked together to form the full 3D image. Interpretation software would identify the surface of the subject within the 3D space of a security screening portal, with the knowledge that millimetre wave penetration of the human body is a small fraction of a millimetre. With a comprehensive simulation capability, optimal

array geometries will be sought which minimise aliasing and enable radiometric sensitivities to approach the 100 mK limit necessary for the detection of many non-metallic threats [2].

2.13 Alternative algorithms for the near-field 3D imaging

The above indicates that for a security screening portal spatial resolution of the order of $\lambda/2$ in 3D would be achievable, which in the millimetre band is between 0.5 mm and 5 mm, which is sufficient for the detection of many threats in a variety of security screening scenarios. This resolution is in excellent agreement with the Abbe resolution limit of microscopy.

The question arises as to whether the Abbe resolution limit for microscopy, applies generally to aperture synthesis microscopy. Aperture synthesis systems might be considered almost equivalent to quasi-optical systems through the Fourier transform relation between the optical transfer function and the point spread function. However, alternative algorithms to invert Eq.1 might be able to reproduce 3D image detail below the diffraction limit. A matrix technique to invert the cross-correlations into a 3D image might offer improved resolution, as a-priori information can be applied to the SVD matrix inversion by setting the threshold values. This capability of imaging in 3D space constitutes a new type of diffractive emission tomography, which will complement existing tomographic techniques, and build on the body of mathematical inversion techniques [20] in imaging science.

Experimental measurements of phase precision of aperture synthesis systems have demonstrated these to be less than a small fraction of a degree. Therefore suitable processing of sub-lambda sampled interference fringes might yield spatial information below the Abbe resolution limit. Such an interferometric aperture synthesis type imaging scheme might be used at lower frequencies in the microwave band where components are cheaper. More generally it might be used at any frequency for 3D imaging, where suitable mixers exist that could shift radiation into the GHz band where signals could be sampled and processed digitally.

3. FUTURE WORK

Future work on the mathematics of inversion of Eq.1 will investigate whether spatial resolutions for an aperture synthesis imaging systems is ultimately determined by the Abbe resolution ($\lambda/2$) limit. On the computational side effort will be concentrated on further development of algorithms to process local visibilities for a security screening portal, seeking to find fast computer memory and CPU efficient processes. These algorithms will then be used in the design of optimal arrays for demonstrators, which will have somewhere in the region of several hundred antenna/receiver channels. The search for funding will continue to develop a portal screening demonstrator.

4. CONCLUSIONS

The generalisation of the 2D radio astronomy imaging technique to one of 3D for the application of a security screening portal has been demonstrated. This generalisation takes the van Cittert Zernike theorem and uses the Fresnel approximation to show how this can be inverted to generate a 3D image from measured cross-correlations. In this generalisation a 3D visibility function was created which was Fourier transformed to create the 3D image. This capability has been demonstrated using simulation to show that a completely new type of emission tomography and 3D microscopy is possible. The technology to realise this would be an array of receivers measuring complex amplitude, a many channel cross-correlator and a PC to run inversion algorithms.

This technique offers a route to processing the aperture synthesis cross-correlations from aperture arrays that are not located in a planar geometry. The antenna/receivers of an envisaged security screening portal could therefore be deployed conformally on surfaces of opportunities, greatly increasing the number of possible deployment scenarios. It also means that antenna/receivers could be conformally bonded into aircraft skins for all-weather imaging. This means that larger collection apertures are possible, providing improved resolution, using hardware which inherently has a small volume, and hence lightweight. It also means that new applications may be possible, perhaps in the field of medicine, to diagnose tissue state using new metrics or measure where established techniques of poor capability.

The Rayleigh spatial resolutions possible with this technique have been demonstrated by simulation to be in the near-field $\lambda/2.09$ m ±10% (close to the Abbe resolution limit of $\lambda/(2.\mathrm{NA})$ metre), typically in the millimetre wave band for security screening between 0.5 and 5 mm. In the far-field the Rayleigh spatial resolution was found to be $\lambda/(1.09D)$ radians ±10%, for an imager aperture size D, (close to that of Fraunhofer diffraction limit) relevant for all-weather imaging. Limitations in the field-of-views of aperture synthesis imagers in the near-field were evaluated and the means

to overcome these presented by processing local visibilities, these will enable imaging in the full 3D space of an envisaged security screening portal.

REFERENCES

[1] Salmon, Bowring, "Near-field and three-dimensional aperture synthesis imaging", SPIE Europe Security+Defence, 'Millimetre Wave and Terahertz Sensors and Technology VI', Dresden, (2013)

[2] Salmon, N.A. et al, "An aviation security (AVSEC) screening demonstrator for the detection of non-metallic threats at 28-33 GHz", ibid

[3] Salmon, N.A. Wilkinson, P.N. and Taylor, C., "Interferometric aperture synthesis for next generation passive millimetre wave imagers", SPIE Europe Security+Defence Europe, 'Millimetre Wave and Terahertz Sensors and Technology V', Edinburgh, September, (2012),

[4] Salmon, N.A., Radiven, J., Wilkinson, P.N., "Amplitude and intensity interferometry using satellite LNB receivers for innovative and low cost microwave and millimetre wave sensor development", ibid

[5] Salmon, N.A., et al, "First video rate imagery from a 32-channel 22-GHz aperture synthesis passive millimetre wave imager', Video rate imagery", SPIE Europe Security+Defence, "Millimetre Wave and Terahertz Sensors and Technology IV", September, (2012), Prague, (2011)

[6] Salmon, N.A. "Minimising the costs of next generation aperture synthesis passive millimetre wave imagers", ibid

[7] Salmon, N.A. Mason, I, Wilkinson, P.N. Taylor, C., Scicluna, P., "First imagery generated by near-field real-time aperture synthesis passive millimetre wave imagers at 94 GHz and 184 GHz", SPIE Europe Security+Defence, "Millimetre Wave and Terahertz Sensors and Technology III", Toulouse, (2010)

[8] van Cittert, P.H. "Die Wahrscheinliche Schwingungsverteilung in Einer von Einer Lichtquelle Direkt Oder Mittels Einer Linse Beleuchteten Ebene", Physica, 1, 201-210, (1934)

[9] Zernike, F. "The concept of degree of coherence and its application to optical problems", Physica, 5, 785-795, (1938)

[10] Born, M, and Wolf, E., "Principle of optics", Cambridge University Press, 7th Edition, (2003)

[11] Thomson, A., Moran, M., Swenson, G, "Interferometry and Synthesis in Radio Astronomy", Wiley, (2004)

[12] Carter, W. "On Refocusing a Radio Telescope to Image Sources in the Near Field of the Antenna Array", IEEE Trans. Antennas & Propagation, vol. 37, No. 3, March, (1989)

[13] Font, J, Camps, A, et al, "SMOS: The Challenging Sea Surface Salinity Measurement From Space", Invited Paper, Proceedings of the IEEE, Vol. 98, Issue: 5, (2010)

[14] Lipson, A, Lipson, S.G., Lipson, H., Chapter 12, "Optical Physics", 4th Ed. , Cambridge Uni. Press, (2011)

[15] Gabriel, C., Gabriel, S., Corthout, E., "The dielectric properties of biological tissue: I. Literature survey", Phys. Med. Biol. 41, pp. 2231-2249, (1996)

[16] Souhmekh, M., "Fourier Array Imaging", Prentice Hall, (1994)

[17] Goodman, "Introduction to Fourier Optics", 3rd Ed., Roberts & Company, (2005)

[18] Papoulis, A., "Systems and Transforms with Applications in Optics", McGraw-Hill, (1968)

[19] Haslam, N.C, Gillespie, A.R. and Halam, C.G., "Aperture Synthesis Thermography – A New Approach to Passive Microwave Temperature Measurements in the Body" IEEE Trans. MTT, Vol. MTT-32, No. 8, pp. 829-835, August, (1984)

[20] Natterer, F., Wübbeling, F., "Mathematical Methods in Image Reconstruction", Monographs on Mathematical Modeling and Computation, Society for Industrial and Applied Mathematics (SIAM), (2001)